5244 *Chem. Mater.* **2009,** *21,* 5244–5251
DOI:10.1021/cm9022612

CHEMISTRY OF MATERIALS
Article

Nanoscale Phase Separation and Building Blocks of $Ge_2Sb_2Te_5N$ and $Ge_2Sb_2Te_5N_2$ Thin Films

Konstantin B. Borisenko,*[,†] Yixin Chen,[†] Se Ahn Song,*[,‡] and David J. H. Cockayne[†]

[†]*Department of Materials, University of Oxford, Parks Road, Oxford, OX1 3PH, United Kingdom, and* [‡]*AE Center, Samsung Advanced Institute of Technology, Yongin, 446-712, Republic of Korea*

Received July 23, 2009. Revised Manuscript Received September 22, 2009

The atomic structures of thin films of nitrogen-doped $Ge_2Sb_2Te_5$ (GST) rapid phase-change memory materials with the general compositions $Ge_2Sb_2Te_5N$ (10% N-GST) and $Ge_2Sb_2Te_5N_2$ (18% N-GST) have been investigated by reverse Monte Carlo refinement based on experimental electron diffraction reduced density functions and density functional theory molecular dynamics simulations. It was found that the nitrogen dopant forms predominantly Ge−N bonds, resulting from nanoscale germanium nitride phase separation during cooling. As in the case of pure GST, the main building blocks of the structure are squares of Ge(Sb)−Te−Sb(Ge)−Te atoms with the contribution from rings containing homopolar Sb−Sb, Te−Te, and Ge−Sb bonds increasing with the nitrogen doping level. These squares are related to the elementary building blocks of the corresponding crystalline structures of the metastable cubic phase of GST. The persistent fragments of the germanium nitride phase are azadigermiridine type N−Ge−Ge−N four-membered rings, with central Ge−Ge bonds. There is an indication from theoretical simulations that two amorphous phases may be present in 18% N-GST, with different bonding types.

Introduction

The $Ge_2Sb_2Te_5$ (GST) chalcogenide glass has become one of the most widely used rapid phase-change memory materials for information storage.[1] The aim, to improve its characteristics for technological applications and also to understand the factors leading to the observed behavior, has sparked an interest into its substituted or doped variants. Previously, properties of several differently doped or substituted GST materials have been investigated both experimentally and theoretically.[2−15] In this paper we focus on nitrogen doped GST.

The main benefit of nitrogen doping in GST would be a reduction in conductivity of the crystalline phase, resulting in smaller currents being needed to read and write information. In a study of the influence of nitrogen doping on GST properties it was observed that small nitrogen doping increased the resistance, while heavy doping decreased the resistance and caused the material to crystallize preferentially in a hexagonal phase.[16] X-ray photoelectron spectroscopy (XPS) measurements of N-doped GST (N-GST) obtained by nitrogen implantation suggest that nitrogen binds preferentially to Ge forming Ge_3N_4.[17] Similarly, several high resolution XPS studies have found the formation of germanium nitride in N-GST along with free N_2 molecules, the latter suggested as existing as interstitials or at vacancy sites or at grain boundaries.[18−24] It was suggested that the formation of germanium nitride is mainly responsible for the observed

*Corresponding authors. E-mail: konstantin.borisenko@materials.ox.ac.uk, sasong@samsung.com.

(1) Ohta, T. *J. Optoelectron. Adv. Mater.* **2001**, *3*, 609.
(2) Qiao, B.; Feng, J.; Lai, Y.; Ling, Y.; Lin, Y.; Tang, T.; Cai, B; Chen, B. *Appl. Surf. Sci.* **2006**, *252*, 8404.
(3) Liu, B.; Song, Z.; Zhang, T.; Feng, S.; Chen, B. *Appl. Surf. Sci.* **2005**, *242*, 62.
(4) Wang, K.; Steamer, C.; Wamwangi, D.; Ziegler, S; Wuttig, M. *Appl. Phys. A: Mater. Sci. Process.* **2005**, *80*, 1611.
(5) Song, W. D.; Shi, L. P.; Miao, X. S.; Chong, T. C. *Appl. Phys. Lett.* **2007**, *90*, 091904.
(6) Park, T.-J.; Choi, S.-Y.; Kang, M.-J. *Thin Solid Films* **2007**, *515*, 5049.
(7) Cai, Y.-F.; Zhou, P.; Lin, Y.-Y.; Tang, T.-A.; Chen, L.-Y.; Li, J.; Qiao, B.-W.; Lai, Y.-F.; Feng, J.; Cai, B.-C.; Chen, B. *Chin. Phys. Lett.* **2007**, *24*, 781.
(8) Ryu, S. W.; Oh, J. H.; Lee, J. H.; Choi, B. J.; Kim, W.; Hong, S. K.; Hwang, C. S.; Kim, H. J. *Appl. Phys. Lett.* **2008**, *92*, 142110.
(9) Song, K.-B.; Sohn, S.-W.; Kim, J.; Kim, K.-A.; Cho, K. *Appl. Phys. Lett.* **2008**, *93*, 043514.
(10) Wang, K.; Steimer, C.; Wamwangi, D.; Ziegler, S.; Wuttig, M.; Tomforde, J.; Bensch, W. *Microsyst. Technol.* **2007**, *13*, 203.
(11) Ling, Y.; Lin, Y.; Qiao, B.; Lai, Y.; Feng, J.; Tang, T.; Cai, B; Chen, B. *Jpn. J. Appl. Phys.* **2006**, *45*, L349.
(12) Choi, K.-J.; Yoon, S.-M.; Lee, N.-Y.; Lee, S.-Y.; Park, Y.-S.; Yu, B.-G.; Ryu, S.-O. *Thin Solid Films* **2008**, *516*, 8810.
(13) Zhou, J.; Sun, Z.; Xu, L.; Ahuja, R. *Solid State Commun.* **2008**, *148*, 113.
(14) Kim, S.-W.; Lim, W.-S.; Kim, T.-W.; Lee, H.-Y. *Jpn. J. Appl. Phys.* **2008**, *47*, 5337.
(15) Shin, H. J.; Kang, Y.-S.; Benayad, A.; Kim, K.-H.; Lee, Y. M.; Jung, M.-C.; Lee, T.-Y.; Suh, D.-S.; Kim, K. H. P.; Kim, C.; Khang, Y. *Appl. Phys. Lett.* **2008**, *93*, 021905.
(16) Kim, S. M.; Shin, M. J.; Choi, D. J.; Lee, K. N.; Hong, S. K.; Park, Y. J. *Thin Solid Films* **2004**, *469−470*, 322.
(17) Liu, B.; Song, Z.; Zhang, T.; Xia, J.; Feng, S.; Chen, B. *Thin Solid Films* **2005**, *478*, 49.
(18) Ling, Y.; Lin, Y.; Lai, L.; Qiao, B.; Lai, Y.; Feng, J.; Tang, T.; Cai, B.; Chen, B. *Integr. Ferroelectr.* **2006**, *78*, 261.
(19) Kim, K.; Park, J.-C.; Chung, J.-G.; Song, S. A.; Jung, M.-C.; Lee, Y. M.; Shin, H.-J.; Kuh, B.; Ha, Y.; Noh, J.-S. *Appl. Phys. Lett.* **2006**, *89*, 243520.
(20) Kim, Y. K.; Baeck, J. H.; Cho, M.-H.; Jeong, E. J.; Ko, D.-H. *J. Appl. Phys.* **2006**, *100*, 083502.
(21) Kim, Y. K.; Jeong, K.; Cho, M.-H.; Hwang, U.; Jeong, H. S.; Kim, K. *Appl. Phys. Lett.* **2007**, *90*, 171920.

Published on Web 10/07/2009

reduction in conductivity.[25] Crystallization was also supposed to become ineffective with the phase separation. Later studies of N-GST using electron energy loss spectroscopy (EELS), however, did not find N_2 molecules in the material.[26] In that study it was shown that, although nitrogen binds preferentially to germanium, distribution of nitrogen throughout the material is homogeneous.

A recent theoretical study of 10 atomic % doped N-GST has found both the germanium nitride and the molecular nitrogen to be present.[27]

Knowledge of the detailed atomic structure of the amorphous phase is essential for understanding the relationship between the observed properties and structure and for designing novel rapid phase-change memory materials with improved properties. In this work we report an investigation into the atomic structure of thin films of amorphous GST doped with 10 and 18 atomic % nitrogen using atomistic model refinements based on experimental electron diffraction data and density functional theory calculations.

Experimental Section

Electron Diffraction Data Collection. Films of amorphous $Ge_2Sb_2Te_5N$ and $Ge_2Sb_2Te_5N_2$ were grown on amorphous SiO_2 films (themselves grown on Si wafers) by DC magnetron sputtering from a target containing commercially available $Ge_2Sb_2Te_5$, while nitrogen was introduced by plasma nitridation during the sputtering. The compositions and stoichiometries of the deposited films were determined by total reflection X-ray fluorescence, inductively coupled plasma, nuclear activation analysis, energy dispersive X-ray analysis, and EELS. The thicknesses of N-doped GST and SiO_2 layers in the deposited films were 300 and 100 nm, respectively. Thin cross-sectional samples for transmission electron microscopy (TEM) were prepared by Ar ion milling of the grown films. Before collecting electron diffraction data, the prepared TEM samples were cleaned in a precision ion polishing system at 2.5 kV to remove surface contamination and any oxidized surface layer.

Electron diffraction patterns from a selected area of approximately 100 nm diameter on the sample were collected using a JEOL 300 kV field emission TEM using a 15 cm camera length. The diffraction patterns were collected using a 1024×1024 pixel CCD camera and were corrected for dark current and pixel sensitivity. Calibration of the scale of the diffraction pattern was performed by recording diffraction patterns of the internal crystalline silicon standard using identical experimental settings. From repeated calibrations, the calibration accuracy was determined to be better than 0.2%, which corresponds to an average error in the interatomic distances of about 0.005 Å. When the random error from fitting is taken into account, the total error in the structural parameters in the present work is estimated to be about 0.01 Å. The center of each diffraction pattern was determined by fitting circles through points of constant diffracted intensity, using code within Digital Micrograph software provided by Dr. T. Petersen.[28] The azimuthally averaged intensity, $I(q)$ (where $q = 4\pi \sin(\theta)/\lambda$ is the scattering vector, θ is the half scattering angle, and λ is the wavelength of electrons), was then used to obtain the reduced scattering intensity, $\phi(q)$, and the reduced density functions (RDF), by techniques described previously.[29−31] Diffraction simulations showed that multiple scattering could be avoided if samples thinner than 5 nm were used. In addition, excellent fitting of the atomic scattering contribution through the oscillations of the total experimental scattering intensity $I(q)$ in the whole range of scattering vector q confirms that the contribution of multiple scattering and energy loss is minimal and can be neglected. In calculation of the RDF curves a damping factor $\exp(-bq^2)$ with $b = 1.0$ Å^2 was used to smooth out oscillations in the curves resulting from the finite extent of q in the experimental reduced scattering intensity data.

Density Functional Theory—Molecular Dynamics and Energy Calculations. A CASTEP density-functional theory software[32] was used to perform molecular dynamics (MD) simulations and energy optimizations using Troullier-Martins pseudopotentials[33] within the generalized gradient approximation (GGA) using the Perdew−Burke−Ernzerhof (PBE) exchange-correlation functional.[34] The good agreement of structures of pure GST computed using these pseudopotentials with experimental data was demonstrated previously.[35,36]

Two cubic cells of N-doped GST, with 71 atoms for $Ge_2Sb_2Te_5N$ and 77 for $Ge_2Sb_2Te_5N_2$ atoms, with random close packing, were first prepared with a density of about 6.0 g/cm^3, intermediate between the density of pure crystalline and pure amorphous GST,[37] since it was supposed that addition of nitrogen would slightly increase the density of the material as compared to that of pure amorphous GST as the nitrogen was assumed to occupy the interstitial and vacancy positions in the atomic framework.[18−24]

Reverse Monte Carlo Refinement. Model structures were refined by comparing $\phi(q)$ calculated from these structures with the experimental $\phi(q)$ using Reverse Monte Carlo (RMC) software similar to that described by McGreevy et al.[38,39] Before the refinement, contributions of the scattering intensity components that gave peaks below 1.1 Å in the experimental RDF, where no contribution from the interatomic distances is expected, were removed using a Fourier filter. In the refinements periodic boundary conditions were used in three dimensions, and a penalty term was added to avoid unphysically close contacts between atoms. This additional penalty function is related to the deviation of the first nearest neighbors in the

(22) Hu, D. Z.; Lu, X. M.; Zhu, J. S.; Yan, F. *J. Appl. Phys.* **2007**, *102*, 113507.
(23) Jung, M.-C.; Lee, Y. M.; Kim, H.-D.; Kim, M. G.; Shin, H. J.; Kim, K. H.; Song, S. A.; Jeong, H. S.; Ko, C. H.; Han, M. *Appl. Phys. Lett.* **2007**, *91*, 083514.
(24) Yin, Y.; Sone, H.; Hosaka, S. J. *Appl. Phys.* **2007**, *102*, 064503.
(25) Raoux, S.; Jordan-Sweet, J. L.; Kellock, A. J. *J. Appl. Phys.* **2008**, *103*, 114310.
(26) Song, S. A.; Zhang, W.; Jeong, H. S.; Kim, J.-G.; Kim, Y.-J. *Ultramicroscopy* **2008**, *108*, 1408.
(27) Sun, Z.; Zhou, J.; Shin, H.-J.; Blomqvist, A.; Ahuja, R. *Appl. Phys. Lett.* **2008**, *93*, 241908.
(28) Petersen, T. Private communication.
(29) Cockayne, D. J. H.; McKenzie, D. R. *Acta Crystallogr., Sect. A* **1988**, *44*, 870.
(30) Cockayne, D. J. H.; McKenzie, D.; Muller, D. *Microanal., Microsc., Microstruct.* **1991**, *2*, 359.
(31) Cockayne, D. J. H. *Annu. Rev. Mater. Res.* **2007**, *37*, 159.
(32) Clark, S. J.; Segall, M. D.; Pickard, C. J.; Hasnip, P. J.; Probert, M. J.; Refson, K.; Payne, M. C. *Z. Krystallogr.* **2005**, *220*, 567.
(33) Troullier, N.; Martins, J. L. *Phys. Rev. B* **1991**, *43*, 1993.
(34) Perdew, J. P.; Burke, K.; Ernzerhof, M. *Phys. Rev. Lett.* **1996**, *77*, 3865.
(35) Hegedüs, J.; Elliott, S. R. *Nat. Mater.* **2008**, *7*, 399.
(36) Borisenko, K. B.; Chen, Y.; Song, S. A.; Nguyen-Manh, D.; Cockayne, D. J. H. *J. Non-Cryst. Solids* **2009**, *355*, 2122.
(37) Njoroge, W. K.; Wöltgens, H.-W.; Wuttig, M. *J. Vac. Sci. Technol. A* **2002**, *20*, 230.
(38) Keen, D. A.; McGreevy, R. L. *Nature* **1990**, *344*, 423.
(39) McGreevy, R. L. *J. Phys.: Condens. Matter* **2001**, *13*, R877.

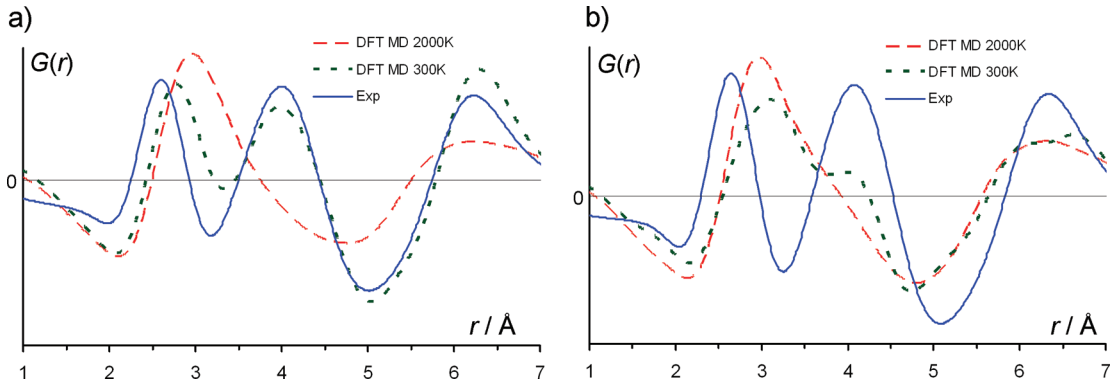

Figure 1. Evolution of RDF from 2000 K to 300 K from molecular dynamics simulations for (a) 10% and (b) 18% N-GST.

model from values used as constraints, which were set to be the sum of the respective covalent radii. By selecting appropriate weighting, this method allowed the atoms to approach each other a little closer than the corresponding sum of covalent radii. In the RMC procedure, a randomly selected atom in the starting atomistic model was moved by a random amount within the specified distance from its initial position. The change in the reduced scattering intensity and its agreement with the corresponding experimental data as well as change in the additional penalty function was then evaluated. If the move improved the agreement it was accepted; if not, the move was accepted with a certain probability. This procedure was repeated until a structure possessing good agreement with the experimental data and also a low additional penalty function value was achieved.

MD Liquid Quench. The refined models were then used as starting structures for melting and cooling simulations using MD within a canonical (constant NVT) ensemble. The models were first melted at 3000 K for 5 ps, then cooled down to 2000 K and equilibrated for 10 ps. The melt was then cooled down to 400 K in steps of 200 K, allowing 5 ps equilibration at each step. Finally, the structures were equilibrated at 300 K for 10 ps. Total simulation time was thus 70 ps with the time step of 2 fs. Although several high frequency modes (for instance, including bonded vibrations) can be anticipated in the materials, a longer time step is used here as a reasonable compromise between describing atomic diffusion and vibrations. This and longer time steps were previously found adequate for simulations of melting and crystallization of pure GST.[35] The temperature was controlled using an implementation of the Nosé-Hoover thermostat.[40] The electron density was sampled only at the gamma point. The pseudopotential energy cut off was set at 200 eV. The models from the final steps of MD simulations were optimized using the relaxation threshold of 1×10^{-5} eV and 500 eV pseudopotential energy cut off. Periodic boundary conditions were used with the lattice constants kept fixed in all optimisations of the models.

Results and Discussion

MD Liquid Quench. The experimental RDF curves for 10% and 18% N-doped GST (Figure 1) are very similar in overall shape, with slight but significant differences in the peak positions.

The RDF curves for 10% and 18% N-GST from the MD simulations, averaged over the simulation time at 2000 K, are also similar to each other. Compared to the curves from MD simulations at 300 K, they have no peak at about 4.0 Å, while the first peak is at a considerably longer distance of about 3.0 Å (cf. 2.5 Å). For 10% N-GST, cooling of the melt results in shortening of the distances contributing to the first peak and formation of the distinct second peak at about 4.0 Å. In the case of 18% N-GST, these changes are not so pronounced.

Comparing the experimental RDF with the MD (300 K) simulations, there is good agreement in overall shape in the case of 10% N-GST (Figure 1a), with the position of the second peak being well reproduced at 4.00 Å and the positions of the third peak being close—6.29 Å in the simulations compared to 6.23 Å for the experiment. There is a larger discrepancy for the first peak position, namely, 2.78 Å in the simulation and 2.60 Å in experiment. For 18% N-GST (Figure 1b), the second peak at 3.99 Å for MD is in relatively good agreement with the experiment at 4.08 Å, but the first peak from the simulation is at 3.09 Å, compared to 2.65 Å in experiment, while the third peak is doubled at 6.14 and 6.62 Å, compared to the experimental peak at 6.34 Å.

The molecular models from the MD (300 K) simulations are shown in Figure 2.

The analysis of the bond type distribution in the simulated models at 2000 K (averaged over the simulation time) and 300 K is shown in Figure 3. Two atoms were considered bonded if the distance between them was shorter than the sum of the respective covalent radii with a 0.5 Å tolerance. It is seen that cooling from the melt to room temperature is accompanied by considerable bond type redistribution. For 10% N-GST the changes include an increase in the number of Ge−Te, Sb−Te, and Sb−Sb bonds, while the number of Ge−Ge, Ge−Sb and Te−Te bonds decrease. In the case of 18% N-doped GST, the contribution of the Ge−N bonds increases considerably. It can be seen from the analysis of bond type distribution that nitrogen preferentially binds to germanium and that there are no N_2 molecules present. While for 10% N-GST the three prevalent bond types are Ge−N, Ge−Te, and Sb−Te, the three prevalent bonds for 18% N-GST are Ge−N, Sb−Te, and Te−Te.

Bond angle distribution analysis was also performed. The angles, formed by two bonds with the same central atom, were found by analyzing the bonding matrix of the models as defined above. In the distribution all possible

(40) Martyna, G. J.; Klein, M. L.; Tuckerman, M. *J. Chem. Phys.* **1992**, *97*, 2635.

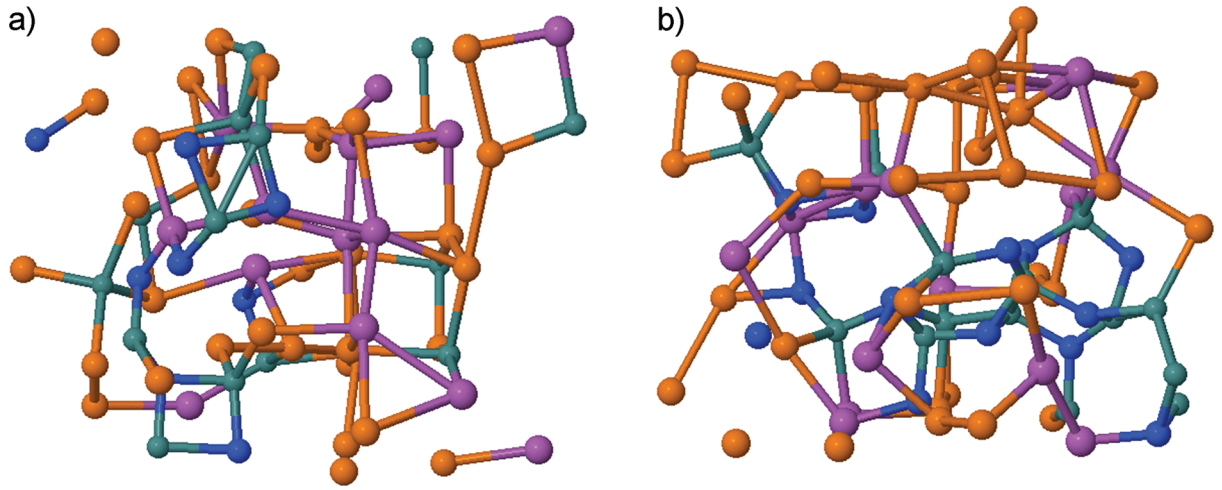

Figure 2. Atomic models of (a) 10% and (b) 18% N-doped GST cooled to 300 K from the melt using molecular dynamics simulations. Ge, green; Sb, lilac; Te, orange; N, blue.

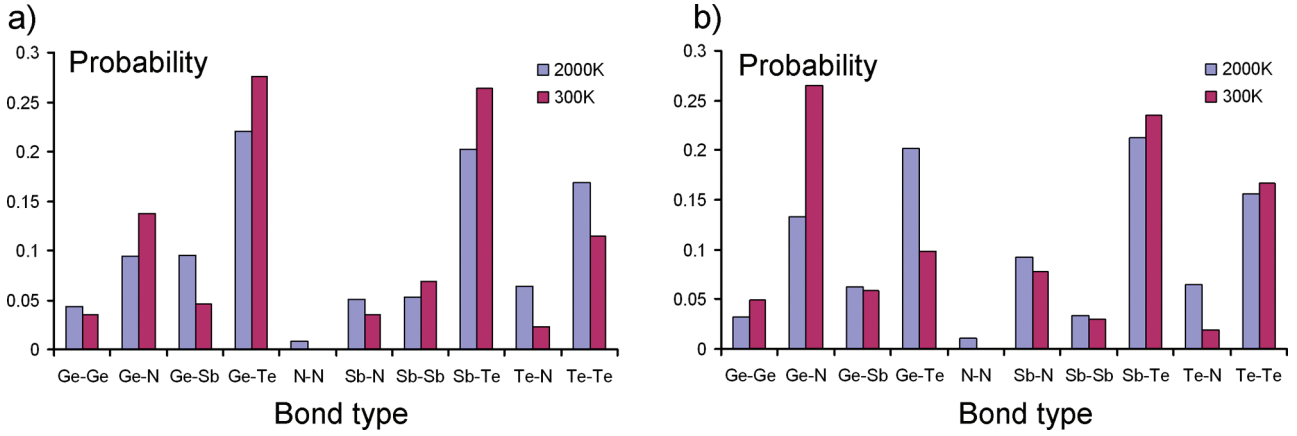

Figure 3. Evolution of bond type distribution from 2000 K to 300 K for (a) 10% and (b) 18% N-GST from molecular dynamics simulations.

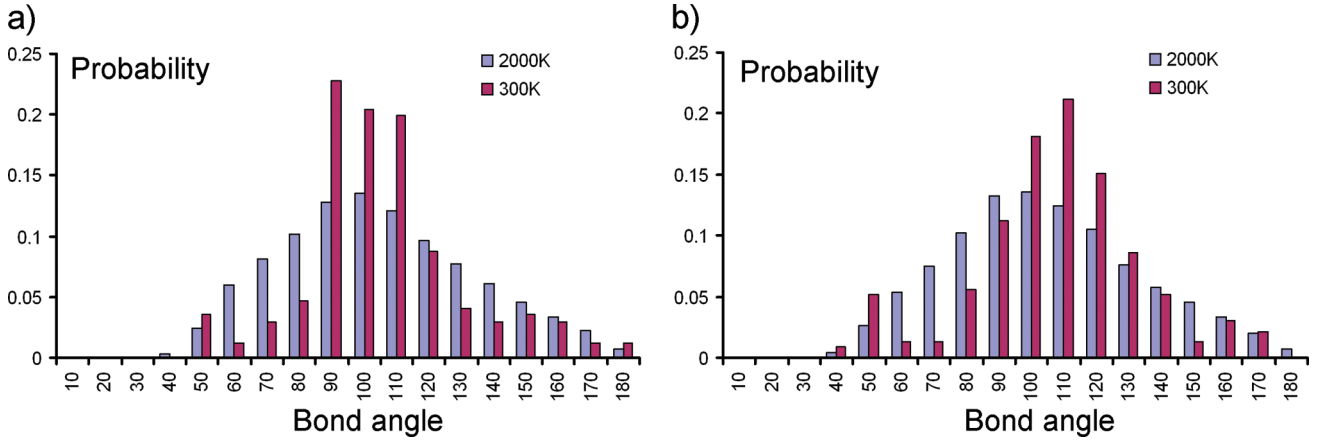

Figure 4. Evolution of bond angle distribution from 2000 K to 300 K for (a) 10% and (b) 18% N-GST from DFT molecular dynamics simulations.

bonded angles were included for all atom types. The bond angle distributions for the two materials (Figure 4) are both centered around 100° at 2000 K. Cooling to 300 K results in a considerable increase in the probability of bond angles near 100° with a shift toward 90° for 10% N-GST, while for 18% N-GST there is also an increase in the probability of bond angles around 100° but with a shift toward 110°. In both cases a peak at 50° appears upon cooling, suggesting that stable three-membered ring structures are formed, with possibly a larger number of such structures in 18% N-GST than in 10% N-GST.

Analyzing models in Figure 2, it is seen that the structures with angles around 90° are planar and distorted four-membered rings. It can also be noted that, unlike pure amorphous GST where these four-membered rings usually include Ge atoms, more such rings contain no Ge for 10%

N-GST. It is even more so for 18% N-GST where these rings mainly consist of Sb and Te atoms, since a larger number of Ge atoms is being bound in nitride form.

Refinement of Close-Packed Models with Energy Optimization. In parallel with the MD simulations, an intitial randomly close packed model with 120 atoms was refined by RMC against the experimental $\phi(q)$, with bonding constraints applied. Eight different sets of bonding constraints were used (see Table 1). The energies of these eight refined models were then optimized in CASTEP by DFT using the same pseudopotentials as in the MD, and the 300 eV pseudopotential energy cut off with full geometry relaxation. This was done to check whether the model obtained by MD was in best agreement (as judged by bond type and bond angle distribution) with that model of the eight which had the lowest energy and/or the best fit to the experimental RDF. This was necessary because the simulation time, compared to real experimental conditions, was relatively short. In addition, it was tested as an alternative to performing computationally demanding MD simulations of liquid quench.

The bonding constraints in Table 1 for both 10% and 18% N-GST reflect the different bonding types that can be encountered in the material, also reflecting the possible phase separations. For example, in the first model (M1), all types of atoms were allowed to come into contact, thus allowing homopolar Ge−Ge, Sb−Sb, Te−Te, and also including Ge−Sb first neighbor contacts having at the same time a completely homogeneous element distribution. In another model of 10% N-GST (M6), homopolar bonds (Te−Te, Sb−Sb) and Te−N and Sb−N bonds were prohibited, while allowing the formation of germanium nitride as observed in the molecular dynamics simulations. It was our observation that models of 18% N-GST without the homopolar Te−Te and Sb−Sb bonds could not be refined. A model including such bonds (M7), however, showed a good agreement with the experimental data after the energy optimisation. Models with N_2 molecules were also tested. Interestingly, the model M8, where the bond type distribution was constrained to that obtained in the MD quench simulations, did not produce a satisfactory agreement with the experiment for either of the materials. We believe that this was due to the fact that different models with constrained and therefore the same bond type distributions will still have different types of bond angle distributions. This will lead to different final structures after the DFT energy optimizations.

For the 18% N-doped GST it is seen that, starting from different initial models, the DFT geometry optimizations converge into stable structures with two considerably different energy levels, with around 150 eV difference (see Table 1). The lower energy structures include models M2 and M3, while the higher energy structures are models M1, M4, M7, and M8. None of the final $G(r)$ curves computed from the lower-energy structures agreed well with the experimental data, whereas some models from the higher-energy structures show much better fit, as indicated by the sum of squared differences, χ^2, shown in the Table 1.

Table 1. Initial Bonding Constraints Applied to the Models of 10% and 18% N-GST with the Corresponding Results of the DFT Energy Optimizations and Comparisons with the Experimental Data

			10% N		18% N	
RMC constraints	bonds allowed	bonds prohibited	total energy (eV)	χ^2 goodness of fit to experimental $G(r)$	total energy (eV)	χ^2 goodness of fit to experimental $G(r)$
M1	Ge−Te, Ge−Sb, Ge−Ge, Sb−Sb, Sb−Te, Te−Te, Ge−N, Sb−N, Te−N, N−N	none	−18880.81	0.159	−21375.48	0.182
M2	Ge−Te, Ge−Sb, Ge−Ge, Sb−Sb, Sb−Te, Ge−N, Sb−N, Te−N, N−N	Te−Te	−18883.74	0.124 **(best $G(r)$ fit)**	−21533.45	0.197
M3	Ge−Te, Ge−Sb, Ge−Ge, Sb−Sb, Sb−Te, Ge−N, Sb−N, Te−N	Te−Te, N−N	−18883.84	0.137	−21535.23 **(lowest energy)**	0.244
M4	Ge−Te, Ge−Sb, Ge−Ge, Sb−Sb, Sb−Te, Te−Te, Ge−N, Sb−N, Te−N	N−N	−18881.18	0.130	−21379.87	0.221
M5	Ge−Te, Ge−Sb, Ge−Ge, Sb−Sb, Sb−Te, Te−Te, N−N	Ge−N, Sb−N, Te−N	−18800.37	0.162		
M6	Ge−Te, Ge−Sb, Ge−Ge, Sb−Te, Ge−N, N−N	Sb−Sb, Te−Te, Sb−N, Te−N,	−18893.90 **(lowest energy)**	0.129 **(good $G(r)$ fit)**		
M7	Ge−Te, Ge−Sb, Ge−Ge, Sb−Sb, Sb−Te, Te−Te Ge-N, N−N	Sb−N, Te−N,			−21374.98	0.179 **(best $G(r)$ fit)**
M8	MD[a]		−18886.08	0.156	−21379.66	0.202

[a] Model M8 is a structure made by applying bond distribution constraints from the results of molecular dynamics liquid quench to the RMC refinements.

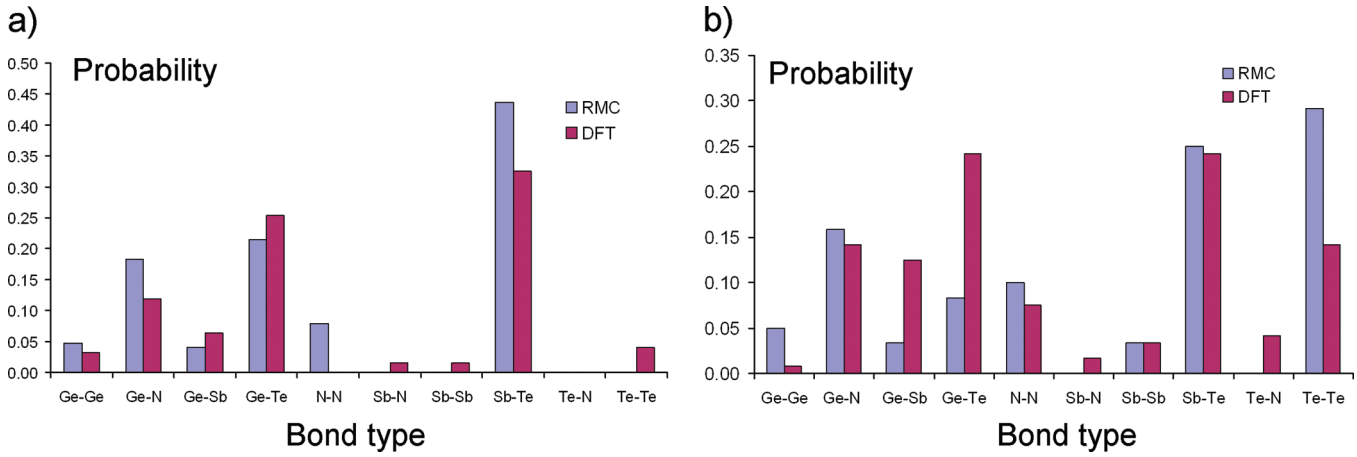

Figure 5. Comparison of bond types distributions before (RMC) and after energy optimization (DFT) for (a) model M6 of 10% N-GST and (b) model M7 of 18% N-GST.

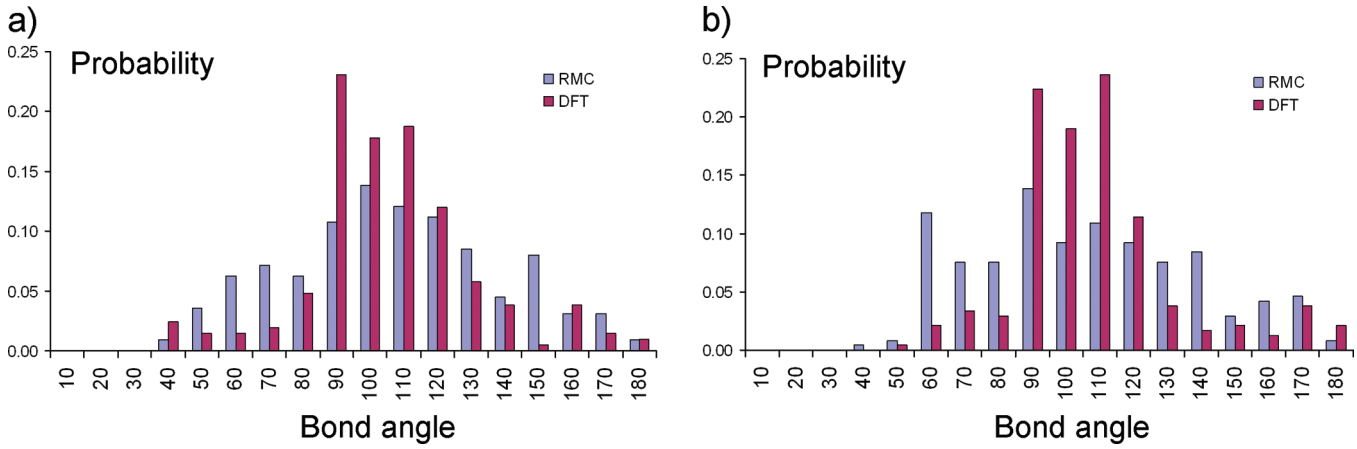

Figure 6. Comparison of bond angle distributions before (RMC) and after energy optimization (DFT) (a) for model M6 of 10% N-GST and (b) for model M7 of 18% N-GST.

The model M6 in Table 1 shows one of the best agreements with the experimental data for the 10% N-doped GST and model M7 has the best fit for the 18% N-doped GST data. Bond type distributions for these models agree with those from the MD simulations in that both show prevailing Ge−N bonds for nitrogen atoms. These models were therefore selected for further structure analysis.

When starting from different initial bonding constraints listed in Table 1 it was observed that the bonding types change dramatically upon energy optimization. In general, for all tested models of N-doped GST, the Ge−Te and Sb−Te bonds predominate, while the numbers of Ge−Ge, Sb−Sb, Sb−N, and Te−N bonds are small in the final energetically stable configurations. Each of these bonds contributes less than 5% of the total number of bonds in the final structures. There is a considerable contribution though of Ge−Sb and Te−Te bonds in the model of 18% N-GST. The changes upon energy optimization for the best fitting models (M6 for 10% N-GST and M7 for 18% N-GST) are shown in Figure 5.

In addition to the bond type distribution, bond angle distributions from RMC refinements showed considerable change upon energy optimization (Figure 6). For model M6 of 10% N-doped GST the angles around 90° are the most abundant. For model M7 of 18% N-doped GST there is a considerable spread of angles about 110°.

Refinement of Large Constrained Models. In the final stages of the study, larger models of about 2000 atoms for both 10% and 18% N-GST were prepared from smaller models obtained in the MD simulations, by assembling the several small models with random orientation, retaining the corresponding structural features of each. In the refinements the bonding constraints from the DFT calculations were preserved as much as possible, including the preferred bond types distribution and bond lengths for each of the bond type by using small displacements of atoms in each of the refinement steps. The results are presented in Figure 7. These refined models not only fit experimental diffraction data well but also retain similar features in bond type and bond angle distributions (Figure 8) to those seen in the quenched models from DFT MD simulations (Figures 3 and 4), that is, increase in the contribution of Ge−N bonds with doping level, predominant contributions of Ge−Te and Sb−Te bonds in the 10% N-GST and increase in contribution of Te−Te bonds in 18% N-GST, and peaks at 50 and 100−110° in

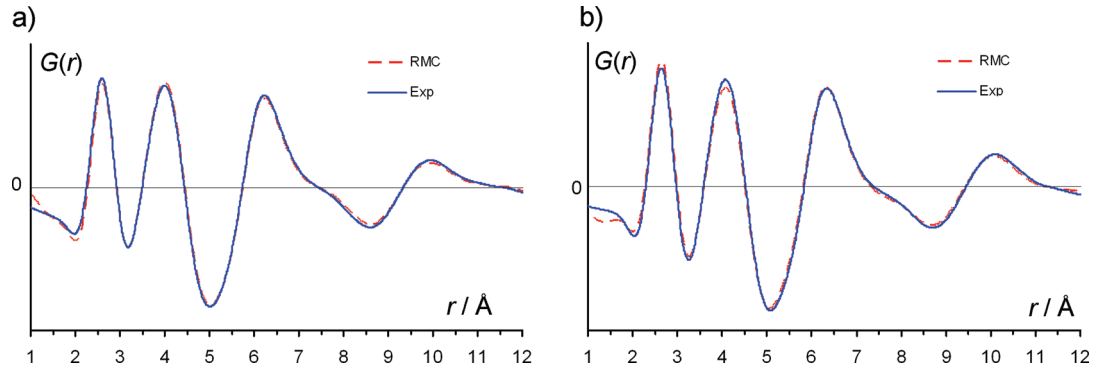

Figure 7. Results of the RMC refinements of large models built from the MD quenched small models for (a) 10% and (b) 18% N-GST.

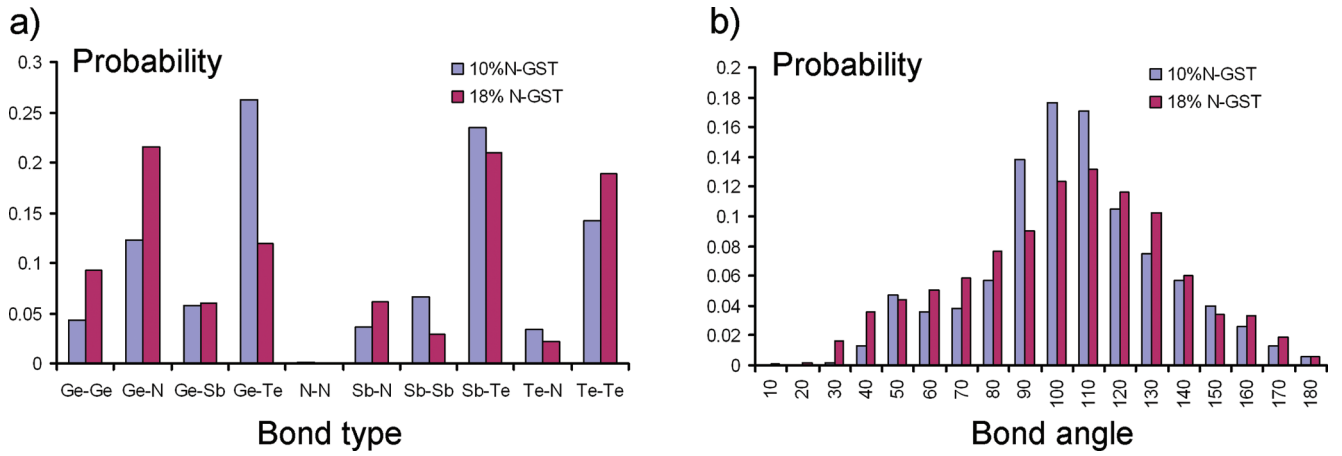

Figure 8. Final (a) bond type and (b) bond angle distributions from the RMC refinements of large models built from the MD quenched small models for 10% and 18% N-GST.

Table 2. Average Bond Distances (Å) and Coordination Numbers from DFT MD Quench at 300 K and Those Obtained in the Constrained RMC Refinements for 10% and 18% N-GST

	10% N-GST		18% N-GST	
parameter	DFT MD	RMC	DFT MD	RMC
Ge−Ge	2.64	2.46	2.55	2.64
Ge−Sb	2.76	2.68	2.67	2.71
Ge−Te	2.63	2.56	2.56	2.50
Ge−N	2.00	1.83	1.94	1.75
Sb−Sb	2.85	2.70	2.95	2.74
Sb−Te	2.89	2.73	2.91	2.70
Sb−N	2.16	2.11	2.24	1.95
Te−Te	2.99	2.73	3.02	2.70
Te−N	2.25	2.16	2.37	2.18
N_{Ge}	4.1	3.9	4.3	5.8
N_{Sb}	3.9	3.3	3.9	3.9
N_{Te}	2.4	2.4	2.6	2.9
N_N	3.1	2.5	3.0	3.0

the bond angle distributions. The average coordination numbers and average bond distances obtained from large refined models are compared with those from the DFT MD quench at 300 K in Table 2.

Figure 9 compares the experimental RDF curves with those from models prepared by random close packing. There is a considerable disagreement in the overall shape of the curves and peak positions, showing that the experimental data does not arise from a randomly packed structure. It is interesting to note that the position of the second peak in the $G(r)$ from random close packing model corresponds to the position of this peak in the melt from MD simulations, as seen in Figure 1. The differentiation of the bonds caused by cooling is due to the chemical short-range order, as has been demonstrated in the MD quench, Figure 3. There is an indication of order at a larger scale of approximately 4−7 Å in comparison between experimental $G(r)$ and the $G(r)$ from random close packing, Figure 9. This ordering is thought to relate to the formation of the stable building blocks in the structures of N-GST as suggested by the formation of the observed patterns in the bond and bond angle distributions after cooling, Figures 3 and 4.

Summarizing the results presented above: through the RMC procedure, model amorphous structures have been constructed consistent with both the experimental diffraction data and quenched models from "molten" structures in the MD simulations. In addition, the energies of the various models have been studied by DFT.

The results of the MD simulations show an increase of the Ge−N bond contribution to the overall bonding after rapid cooling (Figure 3). Bonding consistent with germanium nitride clusters, not predominant in the melt, was found in agreement with previous experimental[17−26] and theoretical[27] observations of a germanium nitride phase in N-GST.

Small but significant differences are observed with increasing N doping. First, both in MD simulations and

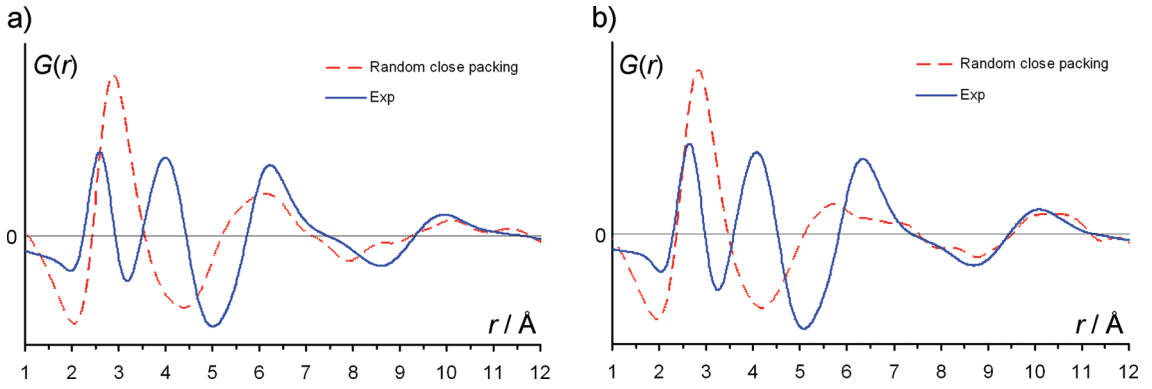

Figure 9. RDF for randomly close packed models of (a) 10% and (b) 18% N-GST.

experiment, there is lengthening, on average, of the shortest bonds. Second, for the higher dopant level, DFT calculations result in the several different starting structures converging to two stable structures with notably different energies. While it is possible that this is an artifact of the small number of atoms in the periodic cell, the observation suggests the possibility of there being two, or even several, energetically stable configurations, possibly with an energy barrier between them which is sufficiently high for the lower-energy structure not to be accessed from the crystallization/amorphization pathway during the phase transition. A common feature of the lower-energy structures is that they have notably fewer Te−Te bonds (3−5%) and notably more Te−N bonds (16−20%) than the higher-energy variants which have 13−18% and 4−10% of these bond types respectively. This suggests that the energy decrease can be correlated to the formation of Te−N bonds and the breaking of Te−Te bonds. And finally, the bond angle distributions suggest that planar and slightly distorted squares and square fragments are the main structural units in the N-doped amorphous GST, as was previously found for pure amorphous GST.[35,36,41] With increase in doping, the increase in the contribution around 50° in bond angle distribution indicates an increase of a N−Ge−Ge−N azadigermiridine[42,43] type structure in a germanium nitride phase.

Although the DFT energy optimizations were useful in producing the energetically stable structures, it was found that a number of different stable models can be computed with different types of bond distribution, depending on the initial starting structure and imposed constraints, all fitting the experimental data reasonably well (Table 1) . Therefore, MD simulations of cooling from the melt may be superior to a set of simple energy optimizations in producing more realistic structures, because these simulations are thought to follow an energy pathway from the melt to the solid state. The MD simulations, as compared to models from energy optimizations (M7) did not show the presence of N−N bonds, which also were not detected in the recent experimental study of N-doped GST.[26]

Conclusion

It has been shown that RMC refinements of the structure of 10% and 18% N-GST based on electron diffraction data when accompanied by theoretical DFT modeling gives a physically meaningful atomistic model of the amorphous phase of the material, which agrees with both experimental data and theoretical calculations. The considerable changes in the bond type and bond angle distributions upon energy optimization indicate the importance of including energy considerations when constructing realistic models of amorphous materials using RMC refinements. Using this approach stable building blocks have been identified that form in the both N-GST structures.

Although the possibility of formation of two different amorphous structures in 18% N-GST will require further experimental and theoretical investigation, such a prospect can open ways to create materials with higher information storage capacity. Knowledge of detailed chemistry and structural features of phase transformation in N-doped GST is an important step in designing novel materials with such properties.

Acknowledgment. K.B.B. and Y.C. thank Samsung for support.

(41) Akola, J.; Jones, R. O. *Phys. Rev. B* **2007**, *76*, 235201.
(42) Tsurnuraya, T.; Sato, S.; Ando, W. *Organometallics* **1990**, *9*, 2061.
(43) Schfer, H.; Saak, W.; Weidenbruch, M. *Organometallics* **1999**, *18*, 3159.